INSTITUTE OF PHYSICS PUBLISHING JOURNAL OF MICROMECHANICS AND MICROENGINEERING

J. Micromech. Microeng. **15** (2005) 1294–1302 doi:10.1088/0960-1317/15/6/022

Comparison of microtweezers based on three lateral thermal actuator configurations

J K Luo[1], A J Flewitt[1], S M Spearing[2,3], N A Fleck[1] and W I Milne[1]

[1] Department of Engineering, University of Cambridge, Trumpington Street, Cambridge, CB2 1PZ, UK
[2] Department of Aeronautics & Astronautics, MIT, Cambridge, MA 02139, USA
[3] School of Engineering Science, University of Southampton, Southampton, SO17 1QJ, UK

Received 26 November 2004, in final form 1 April 2005
Published 16 May 2005
Online at stacks.iop.org/JMM/15/1294

Abstract
Thermal actuator-based microtweezers with three different driving configurations have been designed, fabricated and characterized. Finite element analysis has been used to model the device performance. It was found that one configuration of microtweezer, based on two lateral bimorph thermal actuators, has a small displacement (tip opening of the tweezers) and a very limited operating power range. An alternative configuration consisting of two horizontal hot bars with separated beams as the arms can deliver a larger displacement with a much-extended operating power range. This structure can withstand a higher temperature due to the wider beams used, and has flexible arms for increased displacement. Microtweezers driven by a number of chevron structures in parallel have similar maximum displacements but at a cost of higher power consumption. The measured temperature of the devices confirms that the device with the chevron structure can deliver the largest displacement for a given working temperature, while the bimorph thermal actuator design has the highest operating temperature at the same power due to its thin hot arm, and is prone to structural failure.

(Some figures in this article are in colour only in the electronic version)

1. Introduction

The advance of miniaturization technology has led to the development of microtools which are suitable for precisely manipulating objects at small scales. Applications exist in biomedical and biological fields, micro-assembly of microelectronics, communication devices and precision machining. There is a great demand for microgrippers or microtweezers with a controlled grasping force and accuracy. Such devices must be easy to operate with a large opening displacement at a low power consumption and low temperature. The driving mechanisms used in microtweezers include electrothermal, electrostatic, piezoelectric, pressure and the shape memory effect [1–10]. High voltages of up to hundreds of volts are generally required to operate electrostatically or piezo-electrically driven microtweezers [5, 6], which are thus unsuitable for biological applications. Devices actuated by gas pressure are normally large in size and the device structure is complicated [7]. Shape memory-based devices have problems of low efficiency, limited operating temperature and difficulty in position control [8, 9]. Although these devices are relatively large, with dimensions of up to a few millimetres, only small openings of a few tens of micrometers can be realized. Although microtweezers based on electrothermal actuators need a high current and are usually operated at high temperature [3], they are able to deliver a large force with large opening displacements, and are, therefore, one of the preferred driving mechanisms for microtweezers, especially for non-biological applications. Lateral bimorph thermal actuators based on differential heating

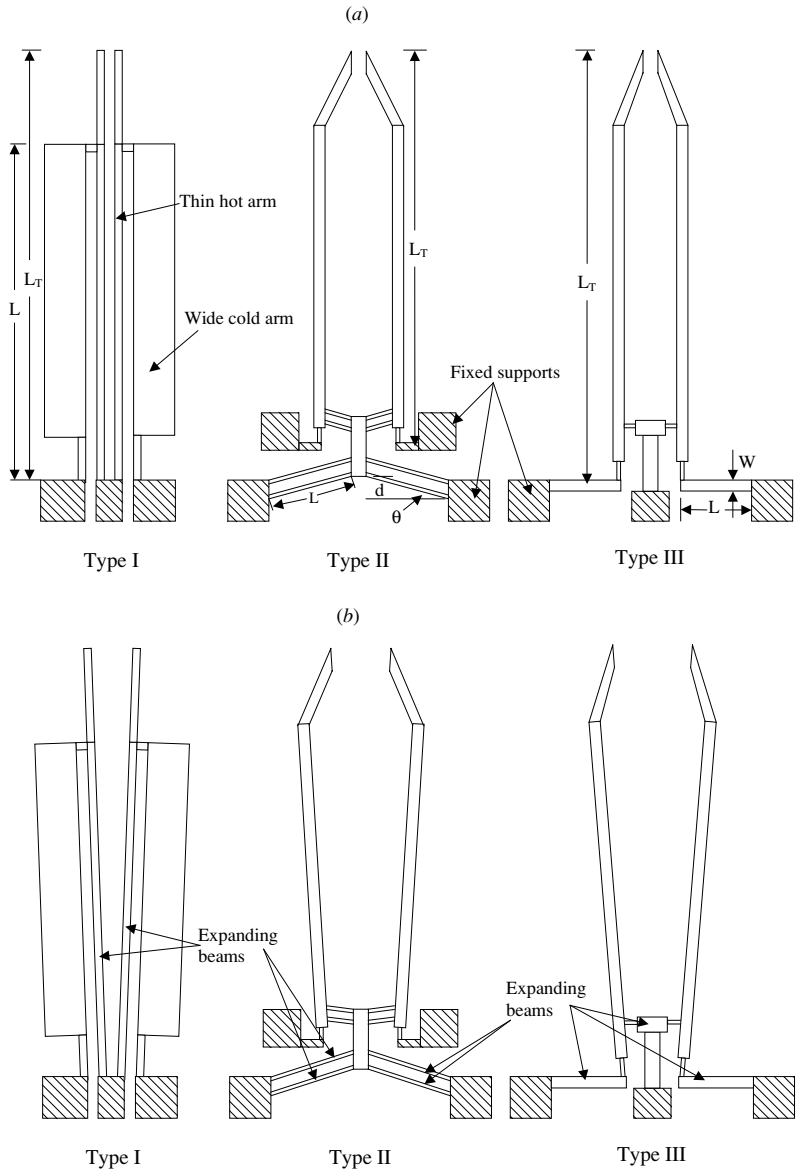

Figure 1. (*a*) Schematic drawings of microtweezers with three thermal actuator structures. The type I device consists of a pair of lateral thermal actuators, the type II device has two inverted chevron actuators while the type III device consists of two horizontal bars, separated from the rotating vertical beams. (*b*) The opening states of microtweezers when they are heated.

achieved through in-plane shape, the so-called 'heatuator', have been widely used as a driving mechanism to generate a large displacement for microtweezers [1, 3]. Much effort has been made to develop this type of microtweezer with a lower operating temperature [10], but little attention has been paid to the optimization of the structure to improve its performance.

Fabrication processes for the aforementioned devices are typically complicated and high-cost [11], and sometimes require special equipment such as a deep reactive ion etcher to etch through Si-wafers [5], or the LIGA process to form a thick layer [11] or special materials [8, 9]. There are great demands for simplified device structures and low-cost fabrication technologies. In this paper, microtweezers employing three types of electro-thermal driving configuration were simulated using finite element analysis, and fabricated using a single mask process based on electroplated Ni films. The performances of these devices were characterized and compared.

2. Design concept

Three types of thermal actuator structure were designed to construct planar microtweezers. All the microtweezers have a total arm length, L_T, of 1100 μm, with an initial tip opening of 20 μm. The type I (figure 1(*a*), left) microtweezer is based on the lateral thermal actuator proposed by Guckel *et al* [1]. It consists of a pair of lateral thermal actuators with hot arms facing each other. Each heatuator has a thin hot arm, a wide cold arm and a hinge. When current passes from one terminal to the other, the thin (high electrical resistance) arm heats more than the wide (low electrical resistance) cold arm. The differential temperature between the hot and cold arms leads to a net expansion of the hot arm, generating a lateral deflection.

The deflection of the heatuator is affected significantly by the widths of the hinge and the hot arm, and the gap between the hot and cold arms [12, 13]. A smaller gap and a narrower beam lead to a larger deflection. In order to produce sufficient force for tweezer applications, the heatuators of the type I microtweezers were designed, with the widths of the hot arm and the hinge 10 μm, the gap 12 μm and a hot arm length 400 μm.

A type II device (figure 1(*a*), middle) consists of a chevron structure fixed by supports on both sides [14, 15]. As current passes through the angled beams, the thermal expansion of these beams leads to an upward deflection of the vertical connection bar (as shown in the figure), which is linked to another inverted chevron structure. The upward-moving vertical bar pushes the inverted chevron upward, and deflects the arms of the microtweezers outward. A number of chevron structures are placed in parallel to increase the force without affecting the flexibility of the individual chevron beams. The deflection of the chevron depends on the inclination angle and the length of the beams of both chevron structures. The smaller the angle, the larger the deflection of the structures [15, 16]. To reduce the lateral dimensions, shorter hot arms (angled beams) of $L = 150$ μm were used for these devices, instead of those of $L = 400$ μm as used in the type I device. The angle of the chevron hot arms is set to be $d/L = 1/10$ for both chevrons (d being the height of a chevron beam as shown in figure 1(*a*)). The length and width of the beams are $L = 150$ and $W = 5$ μm respectively for the large chevron, and $L = 50$ and $W = 4$ μm for the inverted chevron structure.

Configurations I and II produce a deflection at an angle from the direction of the force created by thermal expansion. Therefore, a certain amount of force and power is wasted in converting the force into a deflection. The right-hand drawing of figure 1(*a*) is a schematic drawing of a type III device which uses a driving mechanism proposed by Lin *et al* as a mechanical amplifier to measure the strain [17]. The device has two main horizontal beams, equivalent to the hot arm in a heatuator device, and they are connected with two hinges and a short bar above them. The hinges provide flexibility of rotation for the tweezer's arms. The long and short horizontal bars expand laterally when heated, and deflect the tips of the tweezers outwards. Since the horizontal bars, which generate the thermal expansion, are separated from the tweezer arms, they can be designed to have large dimensions, as the thermal expansion force is proportional to the cross section of the beam. The large dimensions also have the advantage of tolerating a high current without suffering high temperature deformation, which is one of the problems for type I devices, as will be shown later. Similarly shorter horizontal bars with $L = 200$ μm were used for type III devices to reduce the lateral dimension with a width of 20 μm.

3. Finite element simulation

In order to compare the different configurations and their effect on the microtweezer performance, finite element analysis (FEA) based on FEMLAB software (a commercially available plug-in software for MATLAB^{TM} [4]) was used to model the devices. This software has provided an optimal meshing method to secure the accuracy of the simulation with an error of less than 0.1%. In modelling, multi-physics models including plane stress, conductive media dc and heat transfer (solid thermal conduction only) models were used. The heat losses by radiation, convection and conduction via air to the substrate were not considered in the simulation, as the aim was to compare the performance of the devices at the same operation conditions. The Ni properties used in the simulation are listed in table 1 [18–20]. The effect of temperature on the resistivity has been considered in the simulation.

Since the length of the device is much larger than the width and thickness of the devices concerned, the temperature is constant within a cross section of the structure, but varies along the structure, i.e. the direction of the heat flow. Under a steady state, this becomes a classic one-dimensional heat transfer problem. The temperature distribution of the device is known to be independent of the thickness and width [1, 21, 22]. A shape factor was introduced to compensate the effect of the thickness and width [23]. Although the FEA simulation is a two-dimensional modelling, the principle remains unchanged, thus the temperature of the devices is independent of the thickness and width. As we will see from the discussion of section 5, the conductive heat transfer via air to the substrate is the dominant heat loss for these devices; increase in thickness of the device should improve the efficiency of the devices due to the reduced surface to bulk ratio.

Figure 2 shows the simulated tip displacement of all the microtweezers as a function of applied voltage, V. Type II and III devices show better performance in delivering a larger displacement than that of the type I device. The displacement increases parabolically with voltage as predicted by an analytic model [16]. Figure 3 shows the dependence of the displacement against consumed power P_d ($= V^2/R_{d,}$ here R_d is the device resistance). Heatuator-based microtweezers have a small displacement while the other two have similar displacements over the whole power range. It should be pointed out that the lengths of the hot arms are 150 and 200 μm

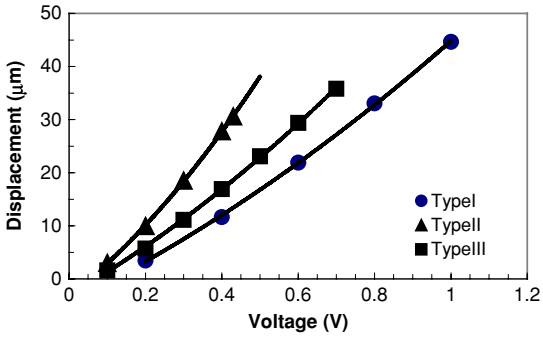

Figure 2. Dependence of the displacement on the applied voltage simulated for three types of device.

Table 1. Material properties of Ni [18, 19].

α 10^{-6} (K^{-1})	ρ 10^{-8} (Ω m)	k (W (m K)$^{-1}$)	E (GPa)	ξ 10^{-3} (K^{-1})
12.7	20	83	210	3.0

[4] The MathWork Inc., 3 Apple Hill Drive, Natick, MA 01760–2090, USA.

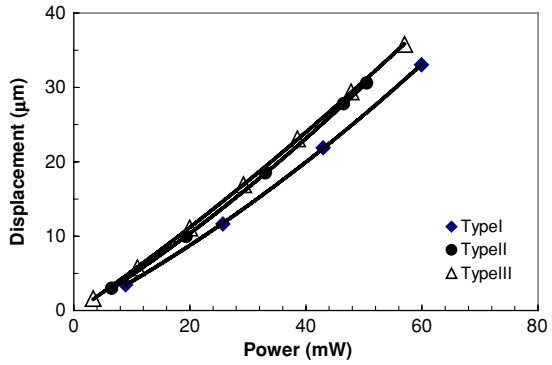

Figure 3. The simulated displacement versus the power consumption for three types of device. The type II and III devices deliver a similar displacement, better than that of the type I device.

for the type II and III devices, which are much shorter than that of the heatuator device (type I) of 400 μm. When a normalized displacement by hot arm length is compared, it is clear that the type II device has the largest normalized displacement, and the type I device has the worst displacement.

4. Fabrication processing

Microtweezers were fabricated using a single mask process on 4″ Si/SiO_2 substrates with a SiO_2 thickness of 100 nm [18, 19]. The structures were formed using a through-mask-plating technology [24, 25]. Figure 4 shows the process flow. A Cr/Cu seed layer with thicknesses of 5/50 nm was deposited by sputtering on a plain Si/SiO_2-wafer, and then the plating patterns were formed by optical photolithography using the photoresist AZ5214E with a thickness of 4 μm as the plating mould. Ni structures were electroplated in a nickel sulphamate solution. The electrical and mechanical properties of electroplated Ni layers have been investigated in detail and reported in [18, 19]. It was found that when it is plated at a current density of 2–4 mA cm^{-2} and at a temperature of 60 °C, the residual stress (uniform stress and stress gradient) of the Ni films is minimal [18, 19]. The typical uniform stress is in the range of ±20 MPa, while the stress gradient is only a few MPa/μm. In order to get a thick Ni structure, a current density of 4 mA cm^{-2} was chosen for all devices here. After plating, the photoresist and seed layer outside the device area were then removed by acetone and chromium etchant, respectively, and the oxide layer was removed by a buffered HF etchant. The actuators were then released by etching the underlying Si using an SF_6 reactive ion etch process with a controlled time. The bond pads have an area larger than 200 × 200 μm^2, much wider than the active structure of the tweezers. When the active structures are released the bond pads remain attached to the Si-substrate. The thicknesses of the Ni films were 3 and 4 μm respectively for the two batches of devices. Figures 5(*a*) and (*b*) show SEM pictures of the electroplated Ni-microstructures. The surfaces of the Ni structures are very smooth and the sidewalls are almost vertical.

Figure 6 shows the three types of released microtweezers and the details of the driving configurations. Although the optimized plating conditions were used to plate Ni films,

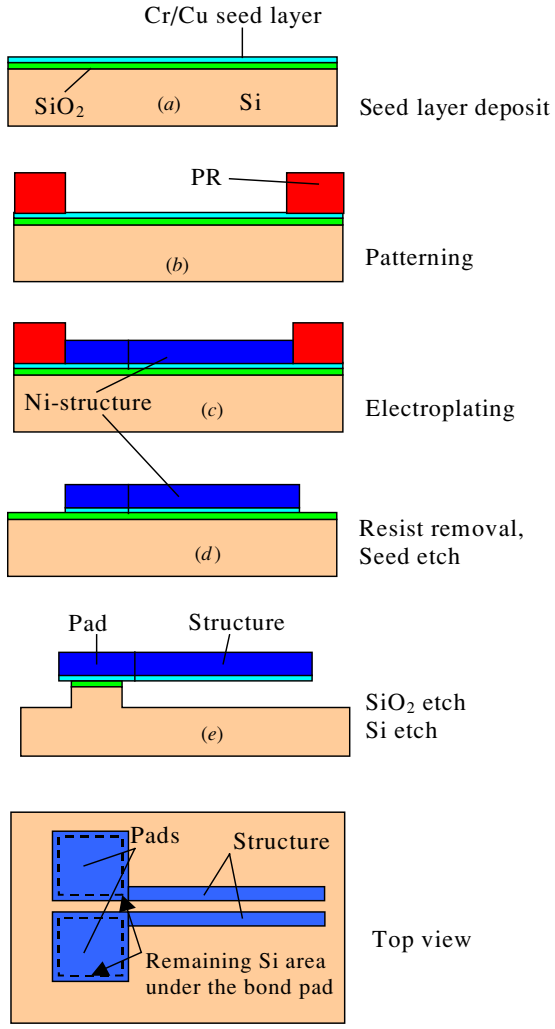

Figure 4. Process flow to make the microtweezers.

minor through-thickness residual stress gradients still existed, leading to a visible out-of-plane deflection of the tips of some tweezers. The residual stress gradient calculated from the tip deflection was less than 1 MPa μm^{-1}, which is consistent with the previous observation [18, 19]. Such small stress gradient has a minor effect on the mechanical properties and device performance [19]. The tensile thermal stress induced by an elevated plating temperature causes the shrinkage of the Ni-beams after their release, leading to an in-plane deflection of the tips for type II & III devices. Hence the tip openings of as-made devices are smaller than those anticipated in the design. This is not a problem for the type I device, as the same shrinkage of the hot and cold arms does not induce a net displacement laterally. Figures 7(*a*), (*b*) and (*c*) show the tip openings after the release process for type I, II and III devices respectively. The opening of the type I device remains the same as originally designed (figure 7(*a*)), whereas the opening of the type III device is much smaller than was designed (figure 7(*c*)), and the tip of the type II device is almost closed with a remaining gap of only about 1 μm (figure 7(*b*)). This effect should be taken into account when designing a real device for a specific application.

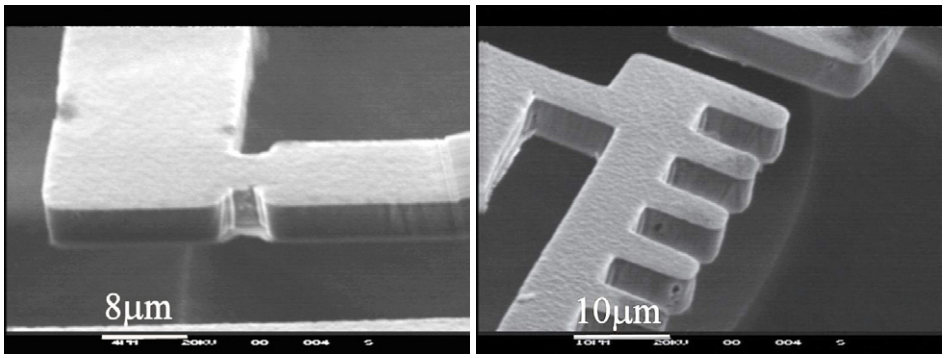

Figure 5. SEM pictures of electroplated Ni microstructures. The surface of the Ni structure is very smooth, and the sidewall is vertical.

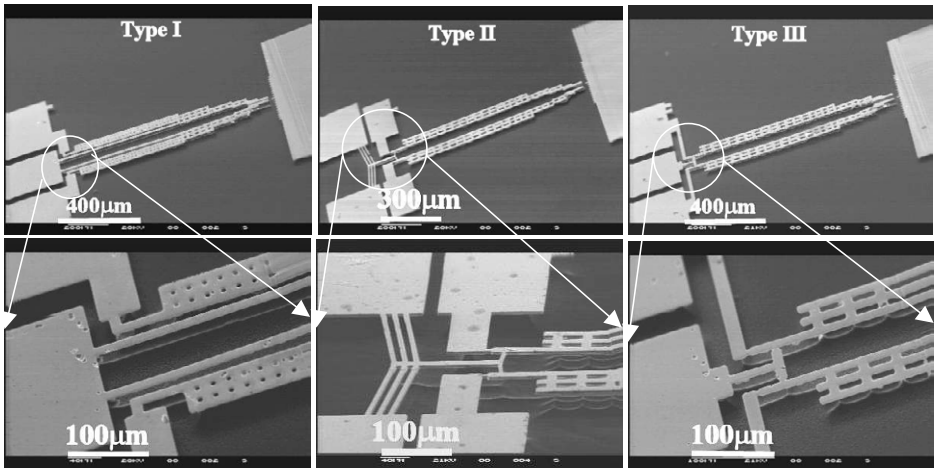

Figure 6. SEM pictures of three types of fabricated microtweezers with insets showing the driving structures.

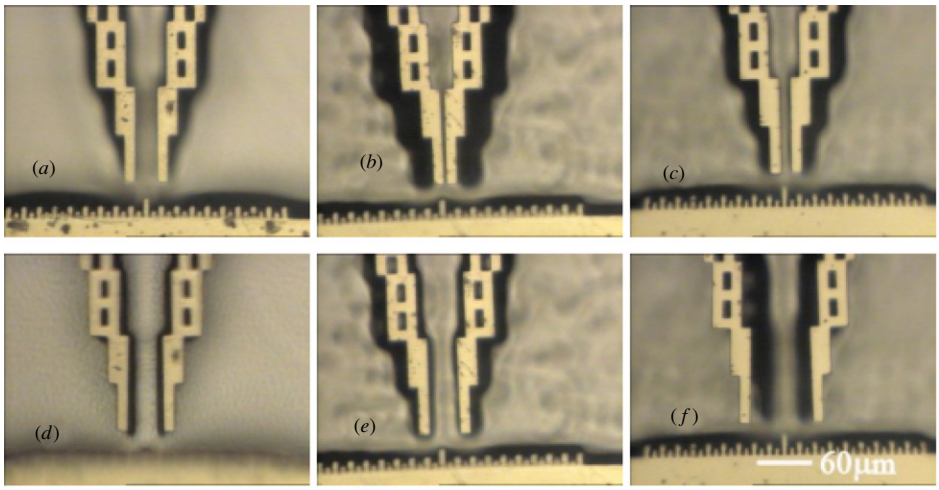

Figure 7. (*a*)–(*c*) Micrographs of type I, II and III microtweezers, respectively. The tip opening of the type I device is 20 μm, while those for the type II and III devices are reduced to 1 and 6 μm due to the tensile thermal stress induced by the elevated temperature plating. (*d*)–(*f*) Micrographs of the type I, II and III devices with applied currents of 95, 260 and 190 mA, respectively.

5. Characterization and discussions

The devices were electrically tested on a wafer on a probe station and were imaged with a video camera. The images of the actuated devices were analysed using commercial image analysis software to obtain accurate measurements of the displacements. A Keithley 2400 Source Meter was used to provide the current and to monitor the voltage simultaneously. To minimize the temperature rise of the device, a pulsed current with a pulse width of 0.3 s was used. Figures 7(*d*), (*e*) and (*f*) are the micrographs of the type I, II and III devices under various currents. Under a current of 95 mA, the type I device produces an opening of 12 $\pm$ 2 μm on one side. Type II and III devices opened up by 15 $\pm$ 2 μm and 30 $\pm$ 2 μm on each

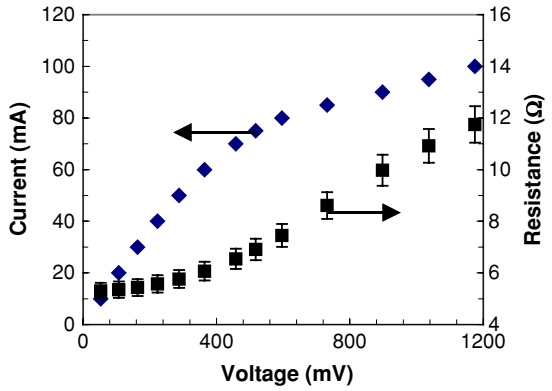

Figure 8. A typical *I–V* characteristic of a thermal actuator (type I). Non-Ohmic behaviour was observed at high currents due to the increased device temperature.

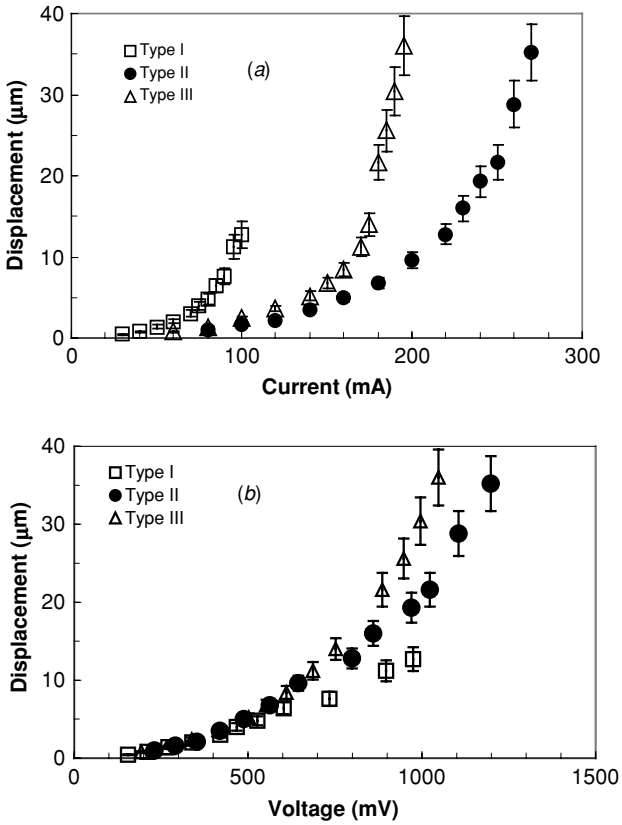

Figure 9. Dependence of the opening of microtweezer tip (one side only) upon the current and voltage for all three types of device.

side at currents of 260 and 190 mA, respectively. The width of the teeth and the gap of the indicator are both 4 μm.

Figure 8 is a typical *I–V* characteristic of a device (a type I device for this figure) together with the resistance. At small voltage ranges, the current increases with voltage linearly and departs from it as the voltage increases further. This is typical non-Ohmic behaviour of a metal resistor. The resistance $R_D(T)$ of a metal device is a function of temperature, to a first-order approximation, $R_D(T) = R_{D0}(1 + \xi(T - T_0))$. ξ is the temperature coefficient of resistivity with a value of 3×10^{-3} K^{-1} for Ni [18, 19].

Figures 9(*a*) and (*b*) show the tip opening (one side only, and the same for all figures shown below) as a

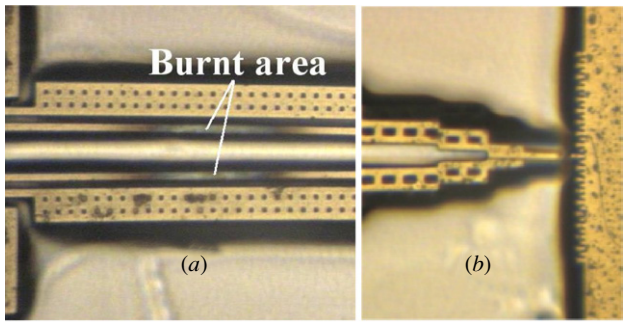

Figure 10. (*a*) Micrograph of failed heatuator hot arms and (*b*) the cross over tips after a measurement at high temperature. The permanent deformation leads to cross over of the tips.

function of voltage and current for all three types of device. The displacements of all devices increase parabolically with increasing voltage and current, in agreement with the analytic model [16]. At a voltage of 1.0 V, the surface of the hot arm of the type I device started to turn brown, and then black. With a further increase in current, the hot arms oxidize severely and creep failure occurs. Figure 10(*a*) shows the thermally damaged hot arms of heatuator tweezers after applying a pulsed current of 100 mA, and 10(*b*) shows the tips crossed over due to creep deformation, a phenomenon observed by other researchers from polysilicon-based heatuators [12, 26]. The tip opening of the type II and III devices continues to increase with further increase in voltage (or current) up to 1.15 V without failure. The current range applicable for a type I device was limited to 100 mA, while it was 290 and 210 mA for type II and III devices respectively.

Due to the different resistances of these devices, the comparison of the performances under a fixed voltage or current is inappropriate. In the following section, the comparison was made using the power consumption and actuation temperature as variables.

The total power used in the measurement is $P = IV$, which includes the power consumed by the parasitic resistance R_P, and by the device resistance, R_D. Because the device resistance is small, typically ~5 Ω as shown in figure 8 at room temperature, the contribution to the total power consumption by parasitic resistances such as the probe, cable resistance and the contact resistance between the probe and bond pads is significant and has to be excluded from the estimate of the power dissipation in the devices. The resistance of a device with several elements of different cross sections is as follows:

$$R_D = \Sigma \frac{\rho L_i}{W_i d} = \frac{\rho}{d} \Sigma \frac{L_i}{W_i} \qquad (1)$$

where L_i and W_i are the length and width of each section, d is the thickness of the Ni film and ρ is the resistivity of the Ni layer. The total measured resistance R_T is the sum of the device resistance and the parasitic resistance, $R_T = R_D + R_P$. The only two unknown parameters, ρ and R_P, can be obtained from the measured total resistances of the three devices. R_P and ρ were found to be $R_P \sim 2 \pm 0.3$ Ω, and $\rho \sim 20 \times 10^{-6}$ Ω cm. The latter is consistent with the previously measured value [18, 19]. The power consumed by the device is $P_D = IV - I^2R_P$. Figure 11 shows the dependence of the displacement against the power consumption P_D for all three

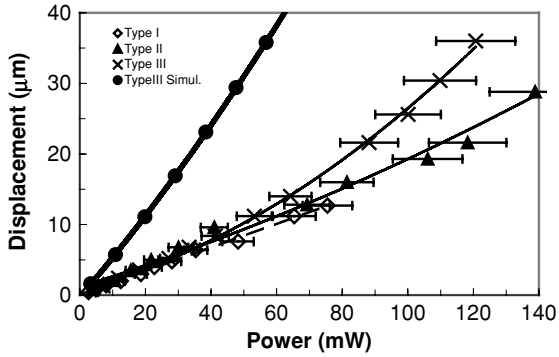

Figure 11. Dependence of the tip opening of the microtweezers upon the power consumption for the three types of device. The type I device is operable only at power levels less than 75 mW, while the other two types of device continue to deliver large displacements at high power. The black dots are the simulated results for a type III device for comparison.

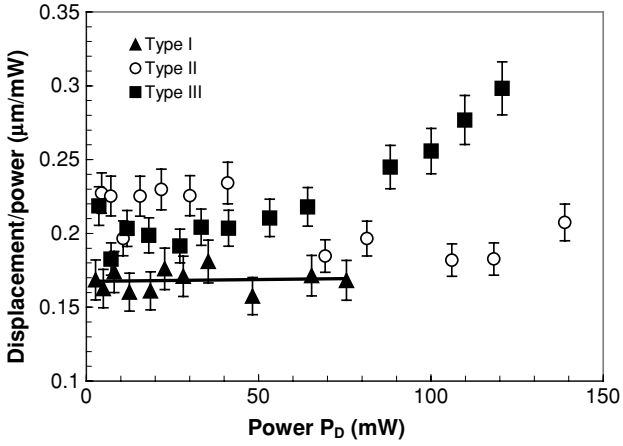

Figure 12. Comparison of displacement per unit power for three types of device. The type II and III devices have a higher displacement per unit power consumption than that of the type I device.

types of device. At low power levels, all devices delivered similar displacements with a slightly better performance for the type III device, in agreement with the modelling results shown in figure 3. At high power ($P_D > 75$ mW), the type I device failed due to thermal damage, while the type II and III devices worked well up to a power of ~120 mW. The displacement increases parabolically with power consumption up to 38 μm, and at the same power level, the type III device had a larger displacement than the type II device. These results have been repeatedly observed in devices from the same batch, and those in another batch with a thinner Ni layer ($d = 3.0\,\mu$m), indicating good reproducibility and repeatability.

The simulated displacements for the type III device are also shown in figure 11 for comparison. The experimental displacements at a fixed power are only 30–40% of the theoretical values. This significant difference is mainly caused by the simplified modelling which did not consider the heat losses by conduction through the air, via convection and radiation. In order to estimate the magnitude of this error, it is useful to consider a 'lumped parameter' model for the system. At a fixed temperature, the power generated by Joule heating P_J is balanced by thermal conduction via the solid beam to the bond pads and the heat losses of thermal conduction via the air to the substrate, convection and radiation via the top surface, which can be expressed as follows [21, 27]:

$$P_J = \left[\frac{k_{sol}A_{sec}}{L} + \frac{k_{air}A_b}{g} + h_{conv}A_t + h_{rad}A_t\right]\Delta T_{ave}\,. \qquad (2)$$

Here k_{sol} (= 83 W (m K)$^{-1}$) and k_{air} (= 0.03 W (m K)$^{-1}$ [21, 27]) are the thermal conductivity of the Ni and air respectively, h_{conv} (= 2–25 W (m^2 K)$^{-1}$ [21]) and h_{rad} the heat transfer coefficients by convection and radiation. g (≈ 25 μm) is the gap between the actuator and the substrate and L is the hot arm length. A_{sec} is the cross section of the hot arm and A_b is the bottom surface area of the thermal actuator. Ignoring edge effects, A_b is the same as the top surface area of the actuator, i.e. $A = A_t = A_b$. ΔT_{ave} is the average temperature of the actuator. Taking half of the type III device as an example, the heat losses can be estimated and compared. The rate of heat transfer by thermal conduction through the solid beam to the bond pads is

$$K_s A_{sec}/L = 83 \times 20 \times 4 \times 10^{-12}/200 \times 10^{-6} = 3.32 \times 10^{-5}\ (\mathrm{WK}^{-1}) \qquad (3)$$

which was the only mechanism considered in the FEA modelling. Other heat losses are all through the surface (the bottom or the top surface) of the actuator, and hence depend on the temperature distribution in the arms of the tweezers. Assuming the temperature of the arm of the tweezer remains at room temperature, the minimum area contributing to the heat losses should be the sum of the main horizontal hot arm and the short bar, and the section between hinge and horizontal bar, which is $A_{min} \approx 4.9 \times 10^{-9}$ m^2. If the heat loss occurs through the arm of the tweezer as well, then the relevant area is roughly five times the minimum area, i.e. $A_{max} = 24.4 \times 10^{-9}$ m^2. The rate of convective heat transfer via the top surface of the actuator is $h_{conv}A = 10 \times (A_{min} \sim A_{max}) = 4.8$–$24 \times 10^{-8}$ W K^{-1}, which is less than 1% of the solid thermal conduction (here $h_{conv} = 10$ is assumed [21]). The radiative heat transfer coefficients, h_{rad}, is a function of temperature. Assuming $\Delta T = 800$ K and that the emissivity is close to unity, the rate of radiation heat transfer corresponding to the minimum and maximum areas is $h_{rad}A = 4$–12×10^{-7} W K^{-1}, which is less than 5% of the solid thermal conduction. On the other hand, the rate of conductive heat transfer via the air to the substrate is given $k_{air}A/g = 5.8 \times 10^{-6}$–$2.9 \times 10^{-5}$ W K^{-1}, which is about 18–88% of the solid thermal conduction. This is likely to be the principal source of the difference between the experimental and simulation results shown in figure 11. The increased importance of gas phase conductive at small scales should be included in future modelling effects. As the conductive heat transfer from the bottom of the structure via air to the substrate is the dominant heat loss, increases in the thickness of the devices will improve the efficiency of the devices.

In order to assess and compare the performance of the three tweezers, the displacement per unit power consumption η of configurations was considered. The displacements per unit power for the three types of device are shown in figure 12 with the consumed power P_D as a variable. Although there is a

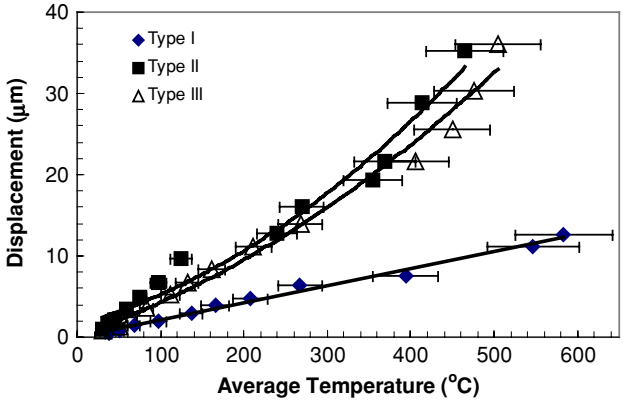

Figure 13. Dependence of the displacement on the measured average temperature of the devices. The type I device has the highest operating temperature but delivered the smallest displacement, while the other two devices have much lower operating temperatures with better displacement performance.

large variation, it is clear that the type I device has the smallest displacement per unit power supplied. At low powers, $\eta \sim 0.17$ μm mW^{-1} for the type I device, while it is $\eta \sim 0.22$ and 0.2 μm mW^{-1} for the type II and III devices. At higher power levels, the displacement per unit power for type II and III devices reached ~0.25 and 0.3 μm mW^{-1} without causing failure, further verifying that the configurations of type II and III devices are better than that of the type I device. This is probably due to the separation of the expansion beams from the tweezer arms and a more uniform temperature distribution, leading to a higher efficiency. Also the maximum temperature for type II and III devices is at a point far away from the tips of the tweezers, whereas it is near to the tips of the tweezers for a type I device.

The temperature of a working device can be extracted through the variation of the resistance with temperature and hence voltage. To a first-order approximation, it can be expressed by

$$\Delta T_{\mathrm{ave}} = T - T_0 = \frac{R_{\mathrm{D}}(T) - R_{\mathrm{D0}}}{R_{\mathrm{D0}}\xi}. \tag{4}$$

Here ξ ($= 3 \times 10^{-3}$ K^{-1} [18, 19]) is assumed to be a constant. The device performance can then be compared using the actuating temperature as a variable, and the results are shown in figure 13. The displacement of the heatuator tweezers is proportional to the average temperature of the device, while the displacements of the other two types of device increase parabolically with the average temperature. The maximum extracted average temperature for the type I device is 585 °C corresponding to a power of 75 mW, much higher than the 465 and 505 °C of the type II and III devices at the highest power shown in figure 13. The heatuator device has the highest actuation temperature, but delivered the smallest displacement. Type II and III devices delivered larger displacements at lower actuating temperatures, indicating their better driving mechanisms.

It is known that the maximum temperature of a beam-like device resistively heated by a fixed voltage across it is related to the average temperature by $T_{\mathrm{max}} = 1.5T_{\mathrm{ave}}$ [16]. The corresponding maximum temperatures are $T_{\mathrm{max}} \approx 878$ °C for a type I device and $T_{\mathrm{max}} \approx 698$ and 758 °C for type II and III devices respectively. This is consistent with the observation that at 878 °C in air, the surface of the Ni will oxidize and significant creep will occur as observed for the type I devices.

It is again worthwhile pointing out that the hot arm length of type I is much larger than those of type II and III devices. It should be straightforward to obtain a comparison of the displacements normalized by the hot arm length, L, from figures 11–13. For instance, the displacements per unit hot arm length are 2, 17.7 and 12%, respectively for type I, II and III devices at 400 °C from figure 13, further indicating that type II and III devices have much higher converting efficiencies than that of type I device. The large gap and wider hot arm are believed to be responsible for the small displacement of the type I device. A large displacement can be achieved for this type of device by using a thinner hot arm with a small gap. However, the temperature concentration or overheating will become serious problems due to the increased resistance of the thinner hot arm, limiting the operating power range and worsening the temperature concentration effect. Also it is difficult to produce a large force using a thinner arm, due to buckling problems. These results imply that the type I device is not suitable for applications with relatively large dimensions. On the other hand, type II and III devices are less prone to buckling, which also results in higher driving forces and better performance.

As can be seen, the devices are operated at a very high temperature, which would cause damage to the devices and the substrate. For practical use, the operation temperature must be reduced significantly by operating it in a pulsed mode or by designing a device using a material with high thermal expansion coefficient. On the other hand, good heat sinks at the end of the tweezers could improve the heat dissipation efficiency, which can be achieved by using large bond pads or using a material with high thermal conductivity such as gold.

6. Conclusions

Microtweezers with three different thermal actuator configurations have been modelled and fabricated using a single mask process and electroplated Ni thin films. A comprehensive characterization and comparison have been made to analyse the device performances through finite element analyses and electrical tests. The microtweezers based on two heatuators deliver the smallest displacement and has a limited power range. This is mainly due to the localized high temperature in the middle of the thin hot arm, leading to failure. Two other types of microtweezer can deliver much large displacements with a higher operating power range, even though they have much shorter hot arms compared to the heatuator device. The actuating temperatures of the thermal actuators were extracted from the variation of resistance under various currents, and these results confirmed that the heatuator device showed the highest actuation temperature at the same power but delivers the smallest displacement, while the devices with the chevron structure have the largest displacement at the lowest temperature. In terms of operating temperature, power range and displacement, the type II and III devices are much better than the type I microtweezers.

Acknowledgment

This research was sponsored by the Cambridge-MIT Institute under grant number 059/P.

References

[1] Guckel H, Klein J, Christenson T, Skrobis K, Laudon M and Lovell E G 1992 Thermo-magnetic metal flexure actuators *Proc. Solid-State Sensor and Actuator Workshop (Hilton Head '92)* pp 73–5

[2] Pan C S and Hsu W Y 1997 An electro-thermally and laterally driven polysilicon microactuator *J. Micromech. Microeng.* **7** 7–13

[3] Larch Ph, Slimane C K, Romanowicz B and Renaud Ph 1996 Modelization and characterisation of asymmetrical thermal microactuators *J. Micromech. Microeng.* **6** 134–7

[4] Ansel Y, Schmitz F, Kunz S, Gruber H P and Popovic G 2002 Development of tools for handling and assembling microcomponents *J. Micromech. Microeng.* **12** 430–7

[5] Volland B E, Heerlein H and Rangelow I W 2003 Electrostatically driven microgripper *Microelectron. Eng.* **61** 1015–23

[6] Carrozza M C, Menciassi A, Tiezzi G and Dario P 1998 The development of a LIGA-microfabricated gripper for micromanipulation tasks *J. Micromech. Microeng.* **8** 141–3

[7] Butefisch S, Seidemann V and Buttgenbach S 2002 Novel micro-pneumatic actuator for MEMS *Sensors Actuators* A **97–98** 638–45

[8] Roch I, Bidaud Ph, Collard D and Buchaillot L 2003 Fabrication and characterisation of an SU-8 gripper actuated by a shape memory alloy thin film *J. Micromech. Microeng.* **13** 330–6

[9] Fu Y Q, Du H J, Huang W M, Zhang S and Hu M 2004 TiNi-based thin films in MEMS applications: a review *Sensors Actuators* A **112** 395–408

[10] Chronis N and Lee L P 2004 Polymer MEMS-based microgripper for single cell manipulation *Proc. 17th Int. Conf. on MEMS (Maastricht)* pp 17–21

[11] Ballandras S, Basrour S, Robert L, Megtert S, Blind P, Rouillary M, Bernede P and Daniau W 1997 Microgrippers fabricated by the LIGA technique *Sensors Actuators* A **58** 265–72

[12] Reid J R, Bright V M and Comtois J H 1996 Force measurements of polysilicon thermal micro-actuators *Proc. SPIE* **2882** 296–306

[13] Moulton T and Ananthasuresh G K 2001 Micromechanical devices with embedded electro-thermal-compliant actuation *Sensors Actuators* A **90** 38–48

[14] Gianchandani Y B and Najafi K 1996 Bent-beam strain sensors *J. Microelectromech. Syst.* **5** 52–8

[15] Que L, Park J S and Gianchandani Y B 2001 Bent-beam electrothermal actuators—part I: single beam and cascaded devices *J. Microelectromech. Syst.* **10** 247–54

[16] Luo J K, Flewitt A J, Spearing S M, Fleck N A and Milne W I 2004 Modelling of microspring thermal actuator *Proc. NSTI-Nanotech (Boston)* vol 1 pp 355–8

[17] Lin L W, Howe R T and Pisano A P 1993 A passive *in situ* micro strain gauge *Proc. 1993 IEEE Micro Electro Mechanical Systems (Ft. Lauderdale, FL)* pp 201–6

[18] Luo J K, He J H, Flewitt A J, Moore D F, Spearing S M, Fleck N A and Milne W I 2004 Development of all metal electro-thermal actuator and its applications *Proc. SPIE* **5344** 201

[19] Luo J K, Flewitt A J, Spearing S M, Fleck N A and Milne W I 2005 Effects of plating process on properties of electroplated Ni-thin films for microsystem applications, unpublished

[20] Sharpe W N Jr 2001 *Mechanical Properties of MEMS Materials* (Baltimore, MD: Johns Hopkins University)

[21] DeWitt I 1996 *Fundamentals of Heat and Mass Transfer* (New York: Wiley)

[22] Huang Q A and Lee N K S 1999 Analysis and design of polysilicon thermal flexure actuator *J. Micromech. Microeng.* **9** 64–70

[23] Lin L W and Chiao M 1996 Electrothermal response of lineshape microstructures *Sensors Actuators* **55** 35–41

[24] Shenoy R V and Datta M 1996 Effect of mask wall angle on shape evolution during through-mask electrochemical micromachining *J. Electrochem. Soc.* **143** 544

[25] Luo J K, Chu D P, Flewitt A J, Moore D F, Spearing S M, Fleck N A and Milne W I 2005 Uniformity control of Ni thin film microstructure deposited by through-mask plating *J. Electrochem. Soc.* **152** C36–41

[26] Deladi S, Krijnen G J M and Elwenspoek M C 2004 Distinction of the irreversible and reversible actuation regions of B-doped poly-Si based electrothermal actuators *J. Micromech. Microeng.* **14** 31–6

[27] Hickey R, Kujath M and Hubbard T 2002 Heat transfer analysis and optimization of two-beam microelectromechanical thermal actuators *J. Vac. Sci. Technol.* **20** 971–4